

Hard X-ray spectroscopy and imaging by a reflection zone plate in the presence of astigmatism

CHRISTOPH BRAIG^{1,*}, HEIKE LÖCHEL¹, ALEXANDER FIRSOV¹, MARIA BRZHEZINSKAYA¹, ALJOSA HAFNER¹, JENS REHANEK², MICHAEL WOJCIK³, ALBERT MACRANDER³, LAHSEN ASSOUFID³, AND ALEXEI ERKO¹

¹Helmholtz-Zentrum Berlin für Materialien und Energie, 12489 Berlin, Germany

²Paul Scherrer Institut, 5232 Villigen PSI, Switzerland

³Argonne National Laboratory, 9700 S. Cass Avenue, Lemont, IL 60439, USA

*Corresponding author: christoph.braig@helmholtz-berlin.de

Compiled November 19, 2015

The feasibility of an off-axis X-ray reflection zone plate to perform wavelength-dispersive spectroscopy, on-axis point focusing and two-dimensional (2D) imaging is demonstrated by means of one and the same diffractive optical element (DOE) at a synchrotron radiation facility. The resolving power varies between 3×10^1 and 4×10^2 in the range from 7.6 keV to 9.0 keV, with its maximum at the design energy of 8.3 keV. This result is verified using an adjustable entrance slit, by which horizontal (H) and vertical (V) focusing to $0.85 \mu\text{m}$ (H) and $1.29 \mu\text{m}$ (V) is obtained near the sagittal focal plane of the astigmatic configuration. An angular and axial scan proves an accessible field of view of at least $0.6 \times 0.8 \text{ arcmin}^2$ and a focal depth of $\pm 0.86 \text{ mm}$. Supported by the grating efficiency around 17.5% and a very short pulse elongation, future precision X-ray fluorescence and absorption studies of transition metals at their K-edge on an ultrashort timescale could benefit from our findings. © 2015 Optical Society of America

OCIS codes: (050.1965) Diffractive lenses; (050.2770) Gratings; (300.6560) Spectroscopy, x-ray; (340.7440) X-ray imaging.

<http://dx.doi.org/10.1364/ao.XX.XXXXXX>

Since their introduction to the X-ray range [1], reflection zone plates (RZPs) have shown their potential as efficient DOEs for monochromatization [2], wavelength selection [3, 4] and one- [5] or two-dimensional (2D) focusing in the soft [6] and hard regime [7] of photon energies. Femtosecond pump-and-probe experiments can be performed with a very short pulse elongation [7], enabling almost Fourier-limited, spatially or time-resolved spectroscopy. However, the combined all-in-one abilities of RZPs were not yet demonstrated until now, in particular in the band between 6 keV and 10 keV, to examine K-edge radiation from transition metals such as Fe, Co, Ni or Cu. In this letter, we report on wavelength-dispersive spectroscopy and imaging with

a resolution down to 20 eV, enabled by a micron-sized focal spot and obtained with the same RZP as it was designed for the preceding proof-of-concept study around $E_0 = 8.3 \text{ keV}$ [7].

For our recent measurements at the 1-BM beamline [8] of the Advanced Photon Source (APS), the off-axis RZP is configured again to operate in its $(-1)^{\text{st}}$ diffraction order and the parameters are adopted from the previous setup [7] with one exception: An open entrance slit presumed in Fig. 1, the X-ray dipole source illuminates the whole RZP now from a distance $R'_{1,\text{ext}} = 34 \text{ m}$ [9, 10]. This enlarged entrance arm length

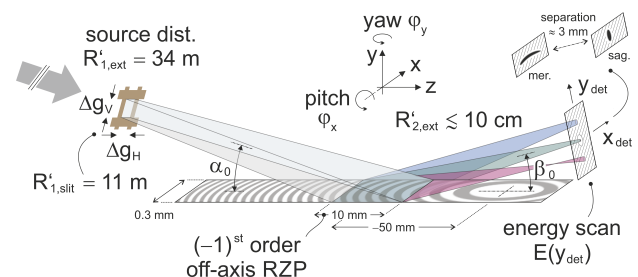


Fig. 1. Experimental setup, as modified from its initial design [7]. The distant source and the maintained incidence angle α_0 lead to an astigmatic focal plane separation by $\approx 3 \text{ mm}$. The exit angle varies around β_0 with the photon energy from $E < E_0$ (red) to $E > E_0$ (blue). The drawing is not to scale.

corresponds to an extension $\Delta R'_1 = 24 \text{ m}$ with respect to the initial value $R'_1 = 10 \text{ m}$. On the other hand, the grazing incidence angle $\alpha_0 = 0.301^\circ$ and its counterpart $\beta_0 = 0.149^\circ$ are maintained within the precision limits of the optics mounting. The focal intensity distribution is hence expected to split up in a sagittal (*s*) and meridional (*m*) plane, slightly displaced from the designed detector position $R'_2 = 0.1 \text{ m}$. We write the sagittal and meridional magnification for the design configuration [7] as $M_{s,m}^{(0)} \equiv Q_{s,m} R'_2 / R'_1$, distinguished by $Q_s = 1$ and $Q_m = \sin(\alpha_0) / \sin(\beta_0)$, respectively. In the new arrangement, the modified ratio $M_{s,m}^{(*)} \equiv [1 + \Delta R'_1 / R'_1]^{-1} M_{s,m}^{(0)}$ – where the

(\star) superscript denotes the extended version with $R'_{1,\text{ext}}$ – is associated with a shift away from the nominal image distance R'_2 toward the RZP, such that the two foci are now expected at

$$R'_{2/s,m}(\star) = [1 + Q_{s,m}(M_{s,m}^{(0)} - M_{s,m}(\star))]^{-1} R'_2. \quad (1)$$

As confirmed by ray tracing, the prediction $R'_{2/s}(\star) = R'_2 - 0.7$ mm from Eq. (1) for a point source and smooth optics is stable under real conditions, whereas a finite source and grating imperfections change $R'_{2/m}(\star) = R'_2 - 2.8$ mm to $R'_2 - 3.6$ mm. An almost point-like symmetry of the well-defined sagittal spot suggests to use the vicinity of this focus for experiments, given by its depth of field of ± 0.86 mm (see below), rather than the meridional one with its broad line shape and much larger axial depth.

To re-investigate the spectroscopic property of the RZP in the off-design operation mode, the X-ray energy is monochromatized to $\lesssim 2$ eV [8] and scanned over an interval of 1.4 keV in steps of 0.1 keV, completed by the reference for E_0 . As shown in Fig. 2, the intensity variation along the dispersive direction y_{det} – denoted by \tilde{y} in the following [7] – is measured by a movable pinhole in front of a photo diode, alike the knife-edge technique. Averaged over the data for the po-

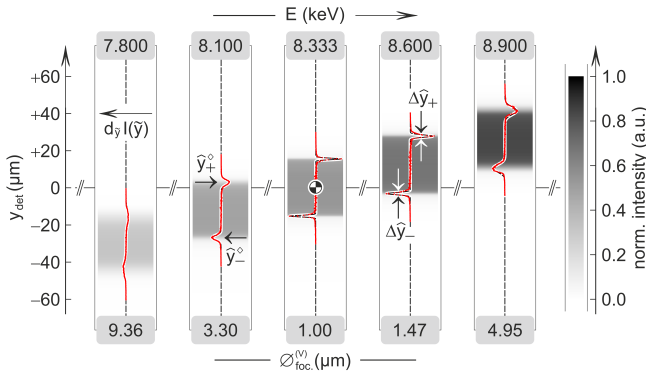


Fig. 2. Selected pinhole edge scan measurements of the full series between 7.6 keV and 9.0 keV. The 1D intensity distribution $I(\tilde{y})$ – spanning an overall dynamic range of 4 due to an energy-dependent RZP efficiency between about 15% and 19% and variable monochromator transmission – is normalized and displayed on a gray scale. Its numerical derivative $d_y I(\tilde{y})$ is shown in red. \hat{y}_{\pm}° and $\Delta \hat{y}_{\pm}$ denote peak positions and widths of the Gaussian fit model (black dashed line), respectively. The 1D spatial resolution $\varnothing_{\text{foc}}^{(V)}$ is listed below.

sition and full width at half maximum (FWHM) of the two peaks at \hat{y}_{\pm}° in Fig. 2 for each one of the 16 scans, the spot size $\varnothing_{\text{foc}}^{(V)}$ as well as the differential dispersion $dE/d\tilde{y}|_{\text{ex}}$ are evaluated. According to Fig. 3, the spectrometer works in acceptable agreement with the grating equation, represented by the proportionality $dE/d\tilde{y}|_{\text{th}} \propto E^2 \sin \beta(E)$ [7]. Via the absolute energy resolution $\Delta E = dE/d\tilde{y}|_{\text{ex./th}} \cdot \varnothing_{\text{foc}}^{(V)}$, Fig. 4 reveals the expected maximal resolving power $\mathcal{R} \equiv E/\Delta E$ in the close vicinity of E_0 . The ray tracing data in Fig. 4 rely on a Gaussian source of $200 \mu\text{m}$ (H) \times $87 \mu\text{m}$ (V) in size [9] and are modeled [7] by $1/\mathcal{R}^2(E) \propto 1 + \mathcal{D}^2(E)$ with $\mathcal{D}(E) \equiv 2\sqrt{3}(E - E_{\star})/\Delta E_{\text{FSR}}^{\star}$ with the peak at $E_{\star} \approx E_0$ and a characteristic width $\Delta E_{\text{FSR}}^{\star} = 0.34$ keV. An rms accuracy of $\pm 6\%$ for this fit to the simulated spectrometer and its noticeable congruence with the empirical curve suggests the proximate validity of the supposed parameters, such that the

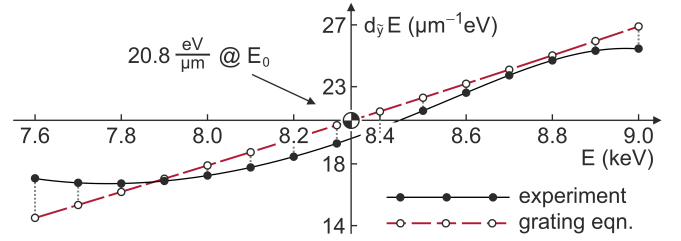


Fig. 3. Measured differential dispersion $dE/d\tilde{y}|_{\text{ex.}}$ (black) as deduced from Fig. 2, compared to the analytical relation $dE/d\tilde{y}|_{\text{th.}}$ (red). Both functions coincide within an error margin of $\pm 6\%$ at E_0 as well as over the full range $7.6 \text{ keV} \leq E \leq 9.0 \text{ keV}$.

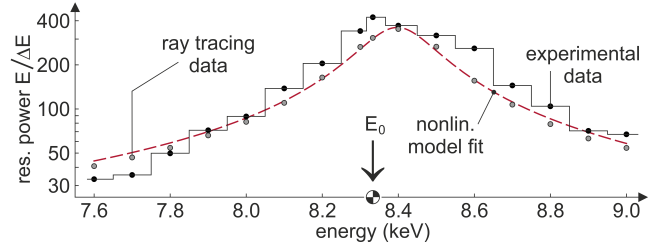


Fig. 4. Resolving power $E/\Delta E$, as evaluated from the spectral scan in Fig. 2 and the dispersion from Fig. 3. Experimental results (black dots with $\pm 1\%$ error bars smaller than symbols, joined to guide the eye) are compared to ray tracing data (gray encircled dots) and the fit model function from [7], in red.

deviations near 7.5 keV, 8.3 keV and around 8.6 keV can be likely ascribed to technical imperfections in angular measurements.

The full flux from the relatively large source is exploited in the spectral scan to illuminate the whole RZP with its efficiency of 17.5%, measured in situ as the ratio between the integrated intensities of the focused and the direct beam. The signal-to-noise ratio of $(1.2 - 2.4) \times 10^2$ comes potentially at the expense of a widened focal spot in comparison to the diffraction limit for a more point-like source. A slit aperture with dimensions $\Delta g_{\text{H}} \times \Delta g_{\text{V}}$ in a distance $R'_{1,\text{slit}} = 11$ m from the RZP, as sketched in Fig. 1, may hence be used to shrink the entrance beam diameter and to control the focus width in consequence. Figure 5 shows the experimental data, taken at E_0 and again determined by the pinhole edge scan method for $10^1 \mu\text{m} \leq \Delta g_{\text{H/V}} \leq 10^3 \mu\text{m}$.

In lateral direction (H), the spatial resolution varies strongly with Δg_{H} – from $0.86 \mu\text{m}$ to $1.47 \mu\text{m}$, while a moderate increase by $0.24 \mu\text{m}$ is observed for $\varnothing_{\text{foc}}^{(V)}(\Delta g_{\text{V}})$. Ray tracing can roughly reproduce the measurements for an assumed detection plane displacement by -0.27 mm from the nominal distance R'_2 and an rms slope error of the RZP that amounts to $\pm 0.65''$ in longitudinal (V) but $\pm 3.82'$ in lateral (H) direction: In conical diffraction, the line edge roughness of the fabricated grooves [7] converts into a source of blurring. In fact, the data are consistent with a universal surface-related contribution $\mathcal{R}_{\text{RZP}} = (0.74 \pm 0.14) \mu\text{m}$ to $\varnothing_{\text{foc}}^{(H)}$ and $\varnothing_{\text{foc}}^{(V)}$, respectively. Its simulated subtraction reveals the undisturbed effect of the decreasing slit width $\Delta g_{\text{H/V}}$, as illustrated in Fig. 5. The homogeneously illuminated RZP operates in its lateral (H) dimension in the regime of geometrical optics, and the constant spatial resolution of $1.36 \mu\text{m}$ (H) is determined by the source size and the de-focused detection plane down to $\Delta g_{\text{H}} \sim 1 \times 10^2 \mu\text{m}$. In the shorter, projected longitudinal (V)

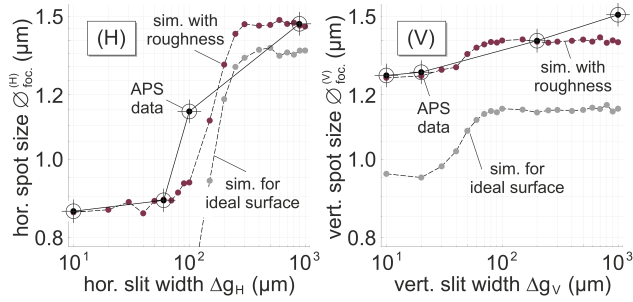


Fig. 5. 1D focus size $\varnothing_{\text{loc}}^{(H)}$ and $\varnothing_{\text{loc}}^{(V)}$ for a variable entrance slit width Δg_H or Δg_V , while the respective other slit dimension is kept at $10^3 \mu\text{m}$. Data points (black) are joined by straight lines to guide the eyes. Ray tracing results are plotted with a slope error (red dashed) and for a smooth surface (gray) of the RZP.

direction, the point spread function (PSF) contributes more influentially an albeit from Δg_V weakly dependent fraction to $\varnothing_{\text{loc}}^{(V)}$ and $1.15 \mu\text{m}$ are maintained until $\Delta g_V \sim 5 \times 10^1 \mu\text{m}$. Below, the grating area tends to "see" a more and more 1D Gaussian-shaped intensity distribution, and the transverse coherence length on the RZP approaches (H) or even exceeds (V) the actually illuminated aperture width or length. As $\Delta g_{H/V}$ shrinks, the pupil at $R'_{1,\text{slit}}$ substitutes the dipole as the operative source. With the reduced extension $\Delta R'_1 \rightarrow 1 \text{ m}$, the astigmatic spots move closer to the designed focal plane by 0.61 mm (*s*) and 2.47 mm (*m*), due to Eq. (1). Finally, beside the roughness, diffraction and the still present astigmatic detection plane mismatch of 0.18 mm in this simulation set a lower bound to $\varnothing_{\text{loc}}^{(H)}$ ($\Delta g_H \rightarrow 0$) $\approx 0.26 \mu\text{m}$ and $\varnothing_{\text{loc}}^{(V)}$ ($\Delta g_V \rightarrow 0$) $\approx 0.96 \mu\text{m}$ in case of perfect optics, or to $0.86 \mu\text{m}$ (H) and $1.26 \mu\text{m}$ (V) for the real sample.

The off-axis RZP works as an imaging lens segment as well. An open entrance slit and the fixed photon energy of 8.3 keV are chosen for convenience. An ANDOR Neo 5.5 sCMOS camera (<http://oxford-instruments.com>) in combination with a scintillator screen and a $10\times$ magnification optics allows for the X-ray detection in the visible wavelength range with an effective pixel size of $0.65 \mu\text{m}$, available over an active sensor area of $1.40 \text{ (H)} \times 1.66 \text{ (V)} \text{ mm}^2$. As shown in Fig. 1, the DOE is rotated around the *x*-axis through the grating center (pitch) over $50''$ in 7 steps and with respect to the *y*-axis (yaw) within $36''$ in increments of $9''$. Taking some sparsity into account, 124 out of 210 peaks in a longitudinal range of 2.4 mm at 6 nearly equidistant *z*-positions around the sagittal focal plane are recorded. 2D Lorentzian shaped profiles describe the intensity distribution of each peak with high accuracy. In general, larger FWHM values than those reported above are observed in this imaging experiment, in part likely caused by multiple scattering in the fluorescent screen along the focus depth of $\approx 6 \mu\text{m}$, from where the magnifying objective ($\text{NA} = 0.3$) collects the photons. The major blurring contribution should be nevertheless ascribed to alignment limitations in this pre-detector optic and the intrinsic camera resolution. It can be modeled simultaneously for both dimensions by a proportional, i.e. non-convolved broadening B_l of the FWHM. Making use of a formal vector notation in

$$[\bar{\varnothing}_{\text{focus}}^{(H,V)}]^2 = B_l^2 \sum_{i=1}^4 [\bar{\varnothing}_{\text{beam}}^{(i)}]^2 \quad \text{with } B_l = 3.9, \quad (2)$$

the (H) and (V) components are composed from the PSF for the source $\bar{\varnothing}_{\text{beam}}^{(i)} \approx M_* Q_{s,m} \bar{\varnothing}_{\text{PSF}}$ [7], its undistorted image size

$\bar{\varnothing}_{\text{beam}}^{(2)} = M_* Q_{s,m} \bar{\varnothing}_{\text{src.}}$, the roughness uncertainty $\bar{\varnothing}_{\text{beam}}^{(3)} \equiv \mathcal{R}_{\text{RZP}}$ and the geometrical propagation term $\bar{\varnothing}_{\text{beam}}^{(4)} \propto |R_{2/s}^{(*)} - R_{2/m}^{(*)}|$, the latter one evaluated to $2.9 \mu\text{m}$. Summed up from these four terms, the theoretical prediction by this simple model agrees with the experimentally determined minimal spot size in the absence of especially pitch- and yaw-induced, i.e. angular, but also other additional aberration effects beyond those taken into account by Eq. (2): From all recorded peaks, $(96 \pm 1)\%$ are larger than $\min\{\bar{\varnothing}_{\text{focus}}^{(H,V)}\} = (3.5 \mu\text{m}, 5.1 \mu\text{m})$ and the rest differs by $\lesssim 2\%$ in its width from this kind of an empirical "lower confidence bound" as the best spatial resolution realized in this imaging performance test. The horizontal spot size statistics in each of these planes are shown in Fig. 6; we derive $\varnothing_{\text{loc}}^{(H)} = (3.6 \pm 0.1) \mu\text{m}$ for $\Delta z_{\text{sag.}} \rightarrow 0$, blurred to at most 120% by definition within the depth of field ($\text{DOF}_{\text{sag.}}$) of $\pm 0.86 \text{ mm}$. In

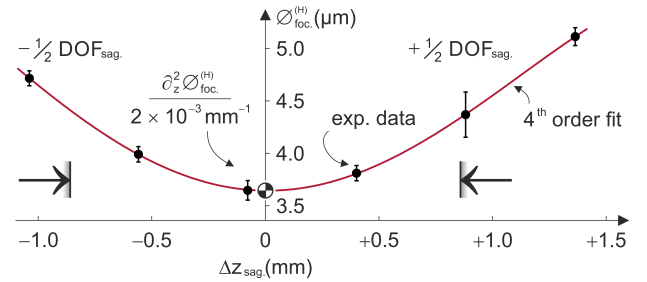


Fig. 6. Horizontal spatial resolution $\varnothing_{\text{loc}}^{(H)}$ with respect to the axial distance $\Delta z_{\text{sag.}}$ from the sagittal plane. Mean data (black dots) with their $\pm \sigma$ uncertainty are fitted by a 4th order polynomial (red). A 20% blurring defines the axial depth $\text{DOF}_{\text{sag.}}$.

contrast, the perpendicular component of the spatial resolution varies in the same axial range $|\Delta z_{\text{sag.}}| \sim \text{DOF}_{\text{sag.}}/2$ on an insignificant level with $\langle \partial_z^2 \varnothing_{\text{loc}}^{(V)} \rangle_{\varphi_{x,y}} = -5 \times 10^{-5} \text{ mm}^{-1}$, averaged over the pitch / yaw range $\varphi_{x,y}$. This curvature is in its absolute value at least $33\times$ weaker than that of $\varnothing_{\text{loc}}^{(H)}$ around $\Delta z_{\text{sag.}} = 0$ (see Fig. 6), can be seen as constant on that scale and is consistent with the astigmatic focal plane separation of a few mm.

The focus position and their relative width, which are of major interest here, remain nonetheless unaffected. In particular, the distribution of the spatial resolution within this 3D scan is evaluated to $\varnothing_{\text{loc}}^{(H)} = (4.2 \pm 0.5) \mu\text{m}$ and $\varnothing_{\text{loc}}^{(V)} = (6.8 \pm 1.2) \mu\text{m}$. A typical result is shown exemplarily for the detection plane nearest to the sagittal one in Fig. 7, i.e. within the innermost $\pm 10\%$ of the axial tolerance $\text{DOF}_{\text{sag.}}$. The spots are tilted versus the \tilde{y} -axis to $\mathcal{V} = 1.7^\circ \pm 10.5^\circ$ – an effect that can be attributed to off-axis aberrations for $\varphi_{x,y} \neq 0$, but in some degree also to the opto-mechanical error budget. Since the actual spatial resolution, which is relevant in real imaging and measured along the principal axes of the spots, differs from the projected values $\varnothing_{\text{loc}}^{(H)}$ and $\varnothing_{\text{loc}}^{(V)}$ by $\lesssim 2\%$, this skew may be neglected in practice.

The angular pitch/yaw variation reveals the reason for the statistical asymmetry between (H) and (V). The peaks keep their on-axis width along x_{det} at least within the yaw range of $\pm 18''$, but are stretched in y_{det} -direction, i.e. for an angular variation $|\varphi_x| \lesssim 25''$. In analogy to the *z*-dependence of the sagittal focal width, the meridional width passes an – albeit weakly pronounced – minimum near $\varphi_x = 10''$, where the overall best resolution $\varnothing_{\text{loc}}^{(V)} = (6.0 \pm 0.1) \mu\text{m}$ is observed. Below and beyond, growing off-axis aberrations restrict the number $N_{\text{FOV}}^{(V)}$ of resolution elements within the 1D spatial field of view (FOV)

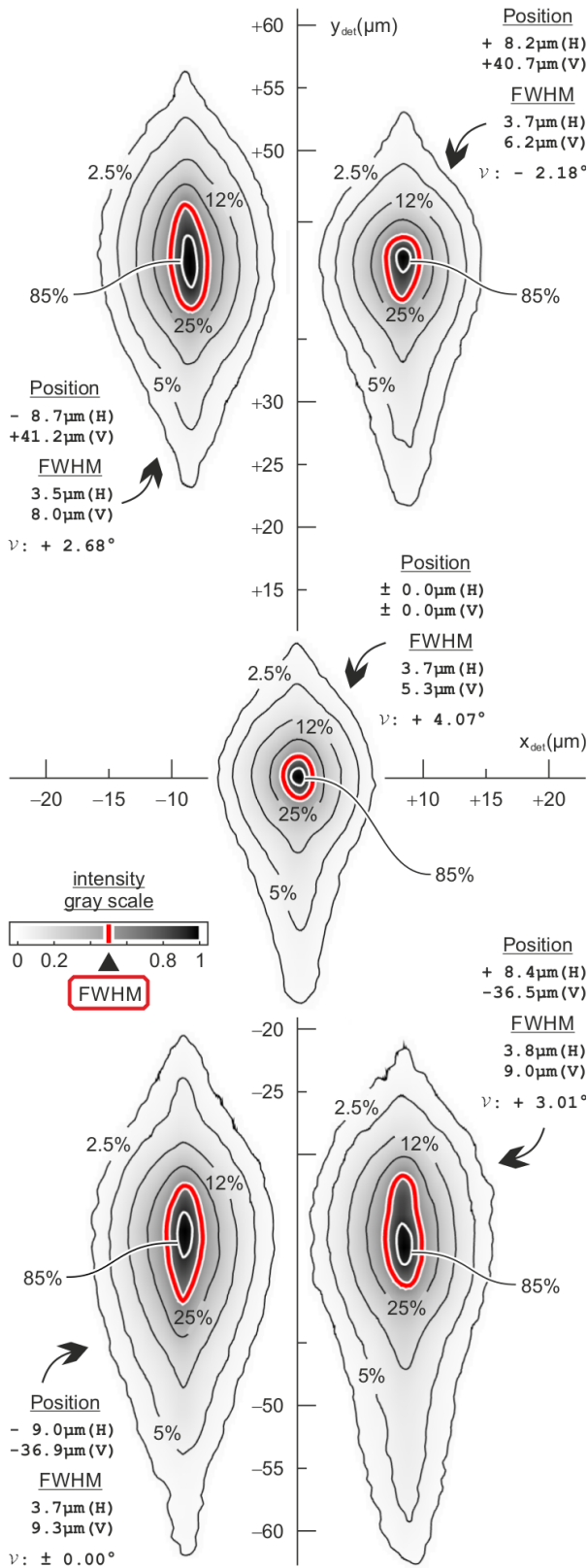


Fig. 7. Scaled 2D intensity distributions over an angular field of view of (0.6×0.8) arcmin² in a distance of $-77.7 \mu\text{m}$ from the sagittal plane (Fig. 6). Gray levels visualize the relative intensity, and the red 50% level contours indicate the FWHM.

$\Delta \bar{y}_{\text{max}}^{(z)}$ for a given z -plane. The hypothetical consideration, that these spots would just also fill that spatial FOV if they were of constant size, can be generalized to the approximated condition

$$N_{\text{FOV}}^{(V)}(\Delta \bar{y}_{\text{max}}^{(z)}) \int_{\Delta \bar{y}_{\text{max}}^{(z)}} \langle \varnothing_{\text{loc}}^{(V)}(\bar{y}_{\text{max}}^{(z)}) \rangle_{\varphi_y} d\bar{y}_{\text{max}}^{(z)} = [\Delta \bar{y}_{\text{max}}^{(z)}]^2, \quad (3)$$

where $\varnothing_{\text{loc}}^{(V)}$ is averaged over the yaw φ_y . We find $\langle N_{\text{FOV}}^{(V)} \rangle_z = 14.8 \pm 1.6$. So, the distortion-limited pitch range $\Delta \varphi_x^{(\text{max})} = (2.0 \pm 0.2)^\circ$ may double the currently covered vertical dimension of the angular field. In the less critical orthogonal direction, an extension up to or even beyond $\Delta \varphi_y \approx \Delta \varphi_x^{(\text{max})}$ can be expected.

In conclusion, three complementary experiments are performed with the same DOE. Spectroscopy with a resolving power $E/\Delta E$ up to 4×10^2 around the Ni K-edge at 8.3 keV, on-axis 2D focusing, unveiling the potential to sub-micron spatial resolution, and depth-scanning imaging over an angular field of $\sim (1 \text{ arcmin})^2$ are, together with the pulse elongation of $\lesssim 1$ fs [7], likely unique in this combination. Transmission zone plates (TZPs) for nano-focusing [11] are limited so far by the aspect ratio to achieve a comparable spectral resolution and efficiency: Diamond [12], Si or Au TZPs require a π thickness up to $10 \mu\text{m}$ – in conjunction with a pitch of $0.1 \mu\text{m}$ or less. In future, our alternative approach may even be optimized, as it should be proven with a custom-made RZP in an adapted setup.

The authors acknowledge funding from the BMBF project "Next generation instrumentation for ultrafast X-ray science at accelerator-driven photon sources" (no. 05K12CB4), a Marie Curie FP7-Reintegration-Grants within the 7th European Community Framework Program (project no. PCIG10-GA-2011-297905) and support by the U.S. Department of Energy, Office of Science, under the contract no. DE-AC-02-06CH11357.

REFERENCES

- V. V. Aristov, S. V. Gaponov, V. M. Genkin, Y. A. Gorbato, A. I. Erko, V. V. Martynov, L. A. Matveev, N. N. Salashchenko, and A. A. Fraerman, *JETP Lett.* **44**, 265 (1986).
- M. Brzhezinskaya, A. Firsov, K. Holldack, T. Kachel, R. Mitzner, N. Pontius, J.-S. Schmidt, M. Sperling, C. Stamm, A. Föhlich, and A. Erko, *J. Synchrotron Rad.* **20**, 522 (2013).
- T. Wilhein, D. Hambach, B. Niemann, M. Berglund, L. Rymell, and H. M. Hertz, *Appl. Phys. Lett.* **71**, 190 (1997).
- C. Braig, H. Löchel, R. Mitzner, W. Quevedo, P. Loukas, M. Kubin, C. Weniger, A. Firsov, J. Rehanek, M. Brzhezinskaya, P. Wernet, A. Föhlich, and A. Erko, *Opt. Express* **22**, 12583 (2014).
- H. Takano, T. Tsuji, T. Hashimoto, T. Koyama, Y. Tsusaka, and Y. Kagoshima, *Appl. Phys. Express* **3**, 076702 (2010).
- M. Källäne, J. Buck, S. Harm, R. Seemann, K. Rossmagel, and L. Kipp, *Opt. Lett.* **36**, 2405 (2011).
- H. Löchel, C. Braig, M. Brzhezinskaya, F. Siewert, P. Baumgärtel, A. Firsov, and A. Erko, *Opt. Express* **23**, 8788 (2015).
- A. Macrander, M. Erdmann, N. Kujala, S. Stoupin, S. Marathe, X. Shi, M. Wojcik, D. Nocher, R. Conley, J. Sullivan, K. Goetze, J. Maser, and L. Assoufid, *AIP Conf. Proc.*, SRI2015 (2015, in press).
- S. Marathe, X. Shi, M. J. Wojcik, N. G. Kujala, R. Divan, D. C. Mancini, A. T. Macrander, and L. Assoufid, *Opt. Express* **22**, 14041 (2014).
- X. Shi, S. Marathe, M. J. Wojcik, N. G. Kujala, A. T. Macrander, and L. Assoufid, *Appl. Phys. Lett.* **105**, 041116 (2014).
- A. G. Michette, S. J. Pfauntsch, A. Erko, A. Firsov, and A. Svintsov, *Opt. Comm.* **245**, 249–253 (2005).
- C. David, S. Gorelick, S. Rutishauser, J. Krzywinski, J. Vila-Comamala, V. A. Guzenko, O. Bunk, E. Färm, M. Ritala, M. Cammarata, D. M. Fritz, R. Barrett, L. Samoylova, J. Grünert, and H. Sinn, *Nature Sci. Reports* **1**, 57 (2011).

REFERENCES

1. V. V. Aristov, S. V. Gaponov, V. M. Genkin, Y. A. Gorbatov, A. I. Erko, V. V. Martynov, L. A. Matveev, N. N. Salashchenko, and A. A. Fraerman, "Focusing properties of shaped multilayer x-ray mirrors," *JETP Lett.* **44**(4), 265–267 (1986).
2. M. Brzhezinskaya, A. Firsov, K. Holldack, T. Kachel, R. Mitzner, N. Pontius, J.-S. Schmidt, M. Sperling, C. Stamm, A. Föhlisch, and A. Erko, "A novel monochromator for experiments with ultrashort X-ray pulses," *J. Synchrotron Rad.* **20**, 522–530 (2013).
3. T. Wilhein, D. Hambach, B. Niemann, M. Berglund, L. Rymell, and H. M. Hertz, "Off-axis reflection zone plate for quantitative soft x-ray source characterization," *Appl. Phys. Lett.* **71**(2), 190–192 (1997).
4. C. Braig, H. Löchel, R. Mitzner, W. Quevedo, P. Loukas, M. Kubin, C. Weniger, A. Firsov, J. Rehanek, M. Brzhezinskaya, P. Wernet, A. Föhlisch, and A. Erko, "Design and optimization of a parallel spectrometer for ultra-fast X-ray science," *Opt. Express* **22**(10), 12583–12602 (2014).
5. H. Takano, T. Tsuji, T. Hashimoto, T. Koyama, Y. Tsusaka, and Y. Kagoshima, "Sub-15 nm Hard X-Ray Focusing with a New Total-Reflection Zone Plate," *Appl. Phys. Express* **3**, 076702 (2010).
6. M. Kalläne, J. Buck, S. Harm, R. Seemann, K. Rosnagel, and L. Kipp, "Focusing light with a reflection photon sieve," *Opt. Lett.* **36**(13), 2405–2407 (2011).
7. H. Löchel, C. Braig, M. Brzhezinskaya, F. Siewert, P. Baumgärtel, A. Firsov, and A. Erko, "Femtosecond high-resolution hard X-ray spectroscopy using reflection zone plates," *Opt. Express* **23**(7), 8788–8799 (2015).
8. A. Macrander, M. Erdmann, N. Kujala, S. Stoupin, S. Marathe, X. Shi, M. Wojcik, D. Nocher, R. Conley, J. Sullivan, K. Goetze, J. Maser, and L. Assoufid, "X-ray Optics Testing Beamline 1-BM at the Advanced Photon Source," *AIP Conf. Proc.*, SRI2015 (2015, in press).
9. S. Marathe, X. Shi, M. J. Wojcik, N. G. Kujala, R. Divan, D. C. Mancini, A. T. Macrander, and L. Assoufid, "Probing transverse coherence of x-ray beam with 2-D phase grating interferometer," *Opt. Express* **22**(12), 14041–14053 (2014).
10. X. Shi, S. Marathe, M. J. Wojcik, N. G. Kujala, A. T. Macrander, and L. Assoufid, "Circular grating interferometer for mapping transverse coherence area of X-ray beams," *Appl. Phys. Lett.* **105**, 041116 (2014).
11. A. G. Michette, S. J. Pfauntsch, A. Erko, A. Firsov, and A. Svintsov, "Nanometer focusing of X-rays with modified reflection zone plates," *Opt. Comm.* **245**, 249–253 (2005).
12. C. David, S. Gorelick, S. Rutishauser, J. Krzywinski, J. Vila-Comamala, V. A. Guzenko, O. Bunk, E. Färm, M. Ritala, M. Cammarata, D. M. Fritz, R. Barrett, L. Samoylova, J. Grünert, and H. Sinn, "Nanofocusing of hard X-ray free electron laser pulses using diamond based Fresnel zone plates," *Nature Sci. Reports* **1**, 57 (2011).